

## Page Proof Instructions and Queries

**Journal Title:** Applied Spectroscopy (ASP)

**Article Number:** 652366

Greetings, and thank you for publishing with SAGE. We have prepared this page proof for your review. Please respond to each of the below queries by digitally marking this PDF using Adobe Reader.

Click “Comment” in the upper right corner of Adobe Reader to access the mark-up tools as follows:

For textual edits, please use the “Annotations” tools. Please refrain from using the two tools crossed out below, as data loss can occur when using these tools.



For formatting requests, questions, or other complicated changes, please insert a comment using “Drawing Markups.”



Detailed annotation guidelines can be viewed at: <http://www.sagepub.com/repository/binaries/pdfs/AnnotationGuidelines.pdf>

Adobe Reader can be downloaded (free) at: <http://www.adobe.com/products/reader.html>.

No.	Query
	Please confirm that all author information, including names, affiliations, sequence, and contact details, is correct.
	Please review the entire document for typographical errors, mathematical errors, and any other necessary corrections; check headings, tables, and figures.
	Please confirm that the Funding and Conflict of Interest statements are accurate.
	Please ensure that you have obtained and enclosed all necessary permissions for the reproduction of artistic works, (e.g. illustrations, photographs, charts, maps, other visual material, etc.) not owned by yourself. Please refer to your publishing agreement for further information.
	Please note that this proof represents your final opportunity to review your article prior to publication, so please do send all of your changes now.
AQ: 1	Please provide title of article
AQ: 2	Please provide title of Book



# Plume Dynamics of Laser-Produced Swine Muscle Tissue Plasma

Joaquin J. Camacho<sup>1</sup>, Luis Diaz<sup>2</sup>, Alicia Marin-Roldan<sup>3</sup>, Samuel Moncayo<sup>3</sup>, and Jorge O. Caceres<sup>3</sup>

## Abstract

We report on the plume dynamics of the plasma induced by laser ablation of a swine skeletal muscle tissue sample in different vacuum conditions. Pulses from a transversely excited atmospheric CO<sub>2</sub> laser were focused onto a target sample and the induced plasma was allowed to expand in different air pressures. The expansion features were studied using fast photography of the overall visible emission by using a gated intensified charged coupled device. Free expansion and plume splitting were observed at different pressure levels. The expansion of the plasma plume front was analyzed using various expansion models and the velocity of the plume front was estimated. The effect of the number of accumulated laser shots on the crater volume at different ambient air pressures and an elemental analysis of the sample were performed using scanning electron microscopy coupled with energy dispersive X-ray spectroscopy analysis. The surface morphology of the irradiated surface showed that increasing the pressure of the ambient gas decreased the ablated mass, or in other words it reduced significantly the laser-target coupling.

## Keywords

Energy dispersive X-ray spectroscopy (EDX), Laser-produced plasma (LPP), Plasma imaging, Scanning electron microscopy (SEM), Shock wave

Date received: 14 May 2015; accepted: 15 October 2015

## Introduction

Laser-produced plasmas (LPPs) are currently a topic of considerable interest in fundamental and applied areas of scientific research. Laser-produced plasmas are transient in nature with characteristic parameters evolving fast in space and time. There are different diagnostic techniques to characterize LPPs such as optical emission spectroscopy, shadowgraphy and fast photography, laser-induced fluorescence, Langmuir probing, photo-thermal beam deflection, mass spectrometry, etc. These studies are essential for understanding various processes in fundamental plasma physics. There are many applications for LPPs in a wide variety of fields of basic research and material technology such as fabrication of thin films by pulsed laser deposition,<sup>1</sup> production of nanoparticles and clusters,<sup>2</sup> surface modifications,<sup>3</sup> spectrochemical analysis of various materials through laser-induced breakdown spectroscopy (LIBS),<sup>4–8</sup> ion source,<sup>9</sup> lithography,<sup>10</sup> microscopy,<sup>11</sup> in the fabrication of micro-electronic devices,<sup>12</sup> etc. Beyond traditional applications of LIBS, where inorganic materials are mainly studied, recent progresses in LIBS lead to analysis of biological warfare agent materials,<sup>13,14</sup> animal tissue studies,<sup>15,16</sup>

biological aerosols,<sup>17</sup> and identification of bacteria.<sup>18</sup> On the other hand, the CO<sub>2</sub> laser has been extensively used over the past 30 years in various fields of medicine<sup>19</sup> and is still one of the most useful and efficient medical lasers available in the market. This laser is mainly employed a surgical or cosmetic tool and can cut or vaporize tissue with fairly little bleeding and minimal damage to surrounding tissue. It is used to remove thin layers from the surface of the skin without going into the deeper layers.

The interaction of a plume with an ambient gas leads to an expansion involving several complex processes such as thermalization, attenuation, deceleration, plasma shielding

<sup>1</sup>Department of Applied Physical Chemistry, Faculty of Sciences, Autonomous University of Madrid, Madrid, Spain

<sup>2</sup>Institute of the Structure of Matter, CFMAC, CSIC, Madrid, Spain

<sup>3</sup>Department of Analytic Chemistry, Faculty of Chemical Sciences, Complutense University of Madrid Madrid, Spain

## Corresponding author:

Joaquin J. Camacho, Department of Applied Physical Chemistry, Faculty of Sciences, Autonomous University of Madrid, Cantoblanco, 28049 Madrid, Spain.  
Email: j.j.camacho@uam.es

of the laser, diffusion, electron-ion recombination, confinement, clustering, and shock wave formation. Recent studies have described a complicated plume-background gas interaction which is characterized by several propagation phases and plume oscillations.<sup>20,21</sup> In recent studies<sup>22</sup> we have studied the emission spectra, electron density, and temperature of laser ablation plumes on swine muscle tissues from spatial and temporal point of view.

In this article, we present an experimental analysis of the laser ablation of swine skeletal muscle tissue by fast photography. This sample was selected due to their similarity in physiological composition with human muscle tissues. Images of the expanding plume were recorded at different vacuum conditions. The plasma was produced by focusing 10.591  $\mu\text{m}$ , 64 ns pulses from a transversely excited atmospheric (TEA)  $\text{CO}_2$  laser on the target at different background air pressures. Fast side-on views of the plume expansion were made by recording overall visible emission from the plasma. This is important for understanding the hydrodynamics of the plume expansion. The dynamic of the plume front was compared with several expansion models finding generally a good agreement. Compared to vacuum, the presence of ambient gas affects significantly the laser-target coupling and the ablated mass. Scanning electron microscopy (SEM) was utilized for high magnification of the laser produced craters and energy dispersive X-ray spectroscopy (EDX) was used to make a quantitative chemical microanalysis of some regions of the sample.

## Experimental

### Sample Preparation

Sample preparation has been previously described elsewhere,<sup>23</sup> thus, only the experimental conditions relevant to the study are presented here. The study was conducted with flesh samples of two pigs obtained from a licensed industrial slaughterhouse with all necessary certificates in compliance with the formal requirements of the European Union. The pigs were not killed only for the purpose of carrying this experiment; rather, they were randomly selected from the stock killed for daily consumption purposes. The spatial inhomogeneity of different elemental concentrations in biological tissues is a well-known phenomenon that can be easily observed by SEM-EDX analysis. In order to lower the impact of spatial inhomogeneity on the samples and to have innocuous and steady biological samples, tissues were lyophilized. A total of 250 mg of tissue were ground using an agate mortar and pestle for 5 min and subsequently compressed into a compact pellet using a hydraulic press at 10 Ton/cm<sup>2</sup>. The thickness and diameter of the pellets were around 2 mm and 13 mm, respectively. The density of the sample was 0.93 g/cm<sup>3</sup>. The pellets were directly analyzed without further preparation.

### Experimental Setup

For producing plasma, 10.591  $\mu\text{m}$ , 64 ns (full width at half maximum [FWHM]) pulses from a TEA  $\text{CO}_2$  laser (Lumonics K-103) were used.<sup>24-27</sup> The ablation pulse energy was fixed at 560 mJ on the sample position measured with a pyroelectric detector (Lumonics 20D), which corresponds to a laser irradiance of 1.1  $\text{GW} \times \text{cm}^{-2}$  ( $70 \text{ J} \times \text{cm}^{-2}$ ). A beam splitter was employed to redirect some small portion of the laser beam to excite a photon drag detector (Rofin Sinar 7415) for temporal shape monitoring and triggering, respectively, through a digital oscilloscope (Tektronic TDS 540). The target was placed in a vacuum chamber achieving a maximum base pressure of  $\sim 7.5 \times 10^{-5}$  Torr (0.01 Pa), and was mounted on a rotating holder to reduce the effects produced by crater formation. The laser beam was focused on the target by a NaCl lens of 24 cm focal length being the measured focused-spot area  $\sim 0.0079 \text{ cm}^2$ . Morphology, chemical elemental composition, and crater size of the laser ablated spots at different vacuum conditions were studied by SEM (Hitachi S-3000N) equipped with EDX analyzer (Oxford Instruments INCAx-sight). Ablation crater depths were measured by using an optical Raman microscope (Renishaw inVia). The plasma emission was collected and imaged onto the open slit of a high-resolution spectrograph with the diffraction grating in zero order (mirror). A quartz Dove prism was inserted into the optical path for rotating the plasma image by 90°, projecting the direction of the plasma expansion (z-axis) onto the entrance slit. The Dove prism is located between two quartz lenses with focal lengths of 80 mm and 40 mm. The magnification of the final image formed by the optical system was found to be 1:0.5. The images were recorded by a gateable intensified charged coupled device (ICCD) (Andor iStar DH-734, 1024  $\times$  1024 pixels, 13  $\mu\text{m}$  pixels). The ICCD detector operating in imaging mode is synchronized with the trigger of the laser pulse.

## Results and Discussion

### Ambient Air Effects on Plasma-Plume Images

When a nanosecond pulsed laser with sufficient energy is focused on a target, ablation of the material and subsequently laser-induced plasma occurs. The initiation of a plasma over the target surface begins in the hot target vapor. The hot vapor plasma-plume interacts with the surrounding atmosphere in two ways:<sup>7</sup> (1) the expansion of the high-pressure vapor produces a shock wave into the atmosphere; and (2) the energy is transferred to the atmosphere by a combination of thermal conduction, radiative transfer, and heating by the shock wave. The relative importance of these processes in determining the subsequent plasma evolution depends on the laser power density, target composition, size of the vapor-plasma bubbles and

focused spot, ambient gas composition and pressure, laser wavelength, and temporal profile. At high irradiance as in this study ( $1.1 \text{ GW} \times \text{cm}^{-2}$ ), shock heating dominates. At long laser wavelengths ( $\lambda > 1 \mu\text{m}$ ) as here, the breakdown initiation is usually associated with cascade ionization ( $h\nu + e + M \rightarrow e^* + M \rightarrow 2e + M^+$ ). The ablated material or dense vapor-plume consists of electrons, ions, atoms, molecules, clusters, and scattered radiation. Clusters are produced due to collective effects and droplets formation is related to hydrodynamics perturbations and big material fragments are ejected due to stress relaxation. Species, which are ejected from the surface, take along some internal and kinetic energy. Initially, the produced species undergo collisions in the high-density region near the target surface, forming the so-called Knudsen layer leading to a highly directional expansion perpendicular to the target. The expansion dynamics of the LPP plume have been described elsewhere.<sup>28</sup> Following the interaction of the laser with the target, it produces an isothermally expanding plasma-plume. This plume absorbs energy from the laser beam and its temperature and pressure grow. An adiabatic expansion of the plasma-plume occurs where the temperature can be related to the dimensions of the plasma.<sup>28</sup>

Plasma emission begins soon after the laser beam reaches the target. The images reported in this study were recorded at different delay time  $t_d$  for a gate width time  $t_w$ , typically of  $0.1 \mu\text{s}$ . Since the number of photons detected in a single-shot image is relatively low, working with gain accumulation of single-shot images allows a more complete image to form. The most significant feature of this approach is the generally large increase in signal-to-noise ratio that is realized, owing to the decrease in the imaging noise. The integration time is properly selected to obtain high quality images depending on different laser parameters and plasma intensity level. Each image represents the spectrally integrated plasma-plume. After a suitable number of laser shots, typically five, the resulting images are ensemble averaged to produce a single representative image. Figure 1 shows time-resolved ICCD images of the expanding plasma produced on a solid swine tissue target at different air pressures ranging from  $7.5 \times 10^{-5}$  Torr to atmospheric pressure. The timings in these images represent the time after the beginning of the laser pulse. At low ambient pressures (Figure 1, top row), due to the low density of the background gas, the interaction of the plume is weak and hence the expansion is mostly perpendicular to the target surface. It is clear that there is not much influence of the ambient air in the expansion of the plasma. The initial plasma shape is elongated ( $t_d < 0.3 \mu\text{s}$ ) and later spherical, due to the radial expanding plasma is not confined by the ambient gas. When the pressure is increased to  $2.8 \times 10^{-2}$  Torr (Figure 1, middle row), the behavior is similar, although the initial elongated shape of the plasma lasts longer ( $t_d < 1.5 \mu\text{s}$ ), owing to the confinement effect induced by

the ambient pressure. At atmospheric pressure (Figure 1, bottom row), the plasma shape is mainly elongated and breaks away from the target surface 200 ns after the onset of the laser pulse, producing a slow movement or a quasi-steady component near the target and another faster moving component. This fast component is slightly out of the laser incident axis. In this case, the plasma behavior is characterized by a strong interpenetration and interaction of the plasma and the ambient high-pressure gas. A contact boundary region is formed between the plasma-plume and the shock wave in the gas. The emission of this fast component exists until  $\sim 5 \mu\text{s}$ . Along with sharpening, the faster component splits again into two clouds. The plume expansion is observed up to  $5.5 \mu\text{s}$  in vacuum ( $7.5 \times 10^{-5}$  Torr) but as the pressure is increased the expansion lasts more time ( $6 \mu\text{s}$  at  $2.8 \times 10^{-2}$  Torr and  $10 \mu\text{s}$  at atmospheric pressure). As the pressure increases, the reciprocal penetration of the plume and the ambient air decreases, producing a confinement of the plume and forming interfaces. In this condition, some turbulence in the expanding plasma also appears along with deceleration and an increase in collisions. This leads to a more and more plasma-plume emission and hence the plumes last longer at high pressures. At these pressures, the expansion dynamics is governed by the nature and pressure of the ambient gas and the plasma shielding of the laser. Plasma shielding is a process in which the laser beam is being prevented from reaching the target by several processes such as inverse bremsstrahlung, ionic, and ionic absorption. The ablated plasma-target surface becomes optically dense at high laser intensities and the tail of the incoming  $\text{CO}_2$  laser pulse may interact with the plasma, being absorbed or reflected.

### Shock Wave Model in Expanding Plasma

The emission intensities of axial area (FWHM) at  $7.5 \times 10^{-5}$  Torr and  $2.8 \times 10^{-2}$  Torr as a function of the delay are given in Figure 2. These graphs are obtained from the images and provide very useful information about the expansion and internal structure of the plasma-plume. When compared over delay time, the averaged images revealed that the plasma emission intensity decay exponentially with time. The plasma size (both axial and radial) at  $7.5 \times 10^{-5}$  Torr grew essentially linear with time (Figure 2, top) while the plasma size at  $2.8 \times 10^{-2}$  Torr follows an anomalous behavior (Figure 2, bottom). At  $2.8 \times 10^{-2}$  Torr, the axial plasma size increases quickly from 0 to  $0.5 \mu\text{s}$  and after it decreases approximately linearly up to  $3.5 \mu\text{s}$  and after increases slowly up to  $5 \mu\text{s}$ . This behavior can be due to the interaction of the LPP with air background dragging the expansion of the plasma. This is due to various complex interactions taking place between the expanding plasma species and the background gas species at different pressure levels. Compared with vacuum (Figure 1,

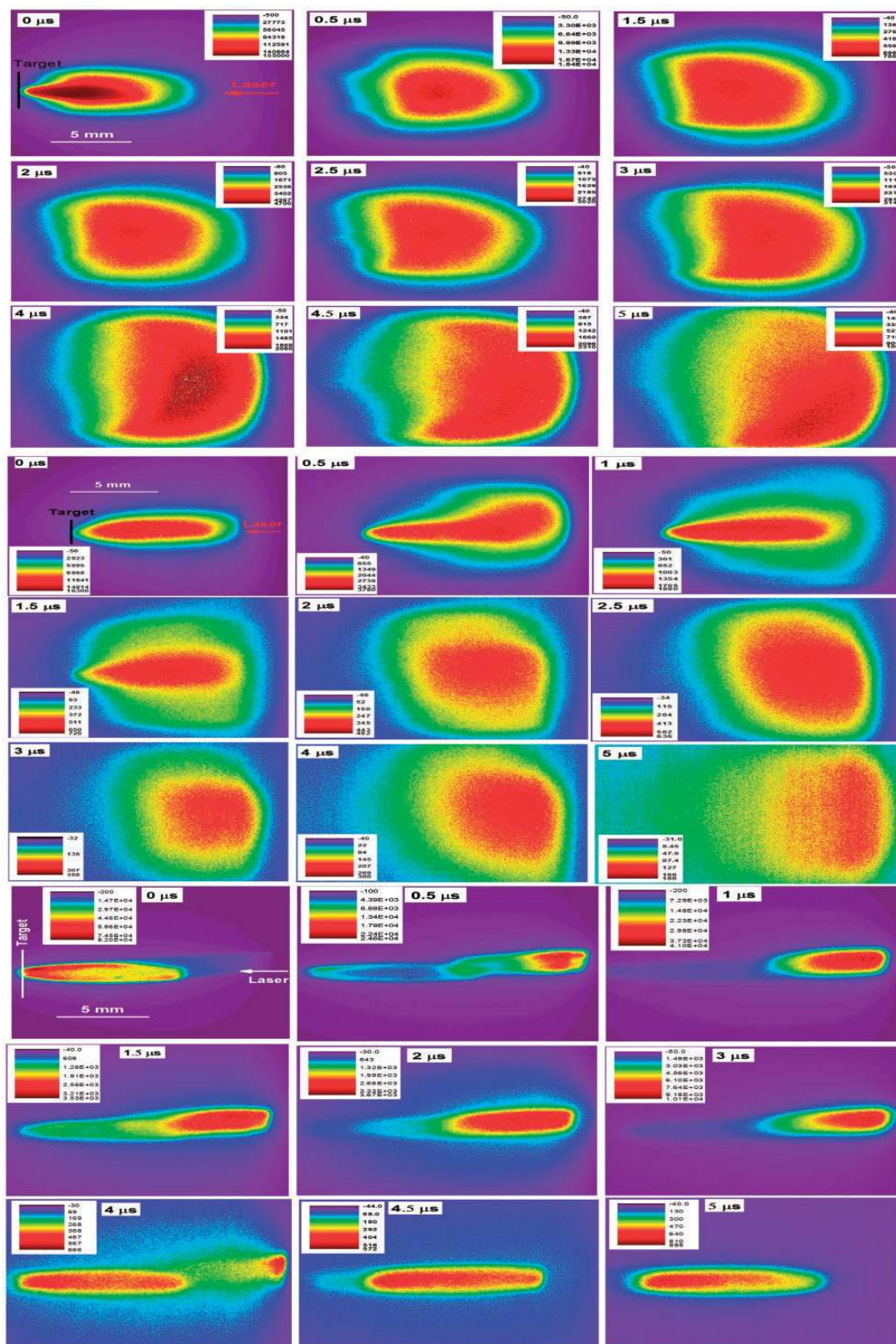


**Figure 1.** Time-resolved ICCD images of swine tissue at different background pressures:  $7.5 \times 10^{-5}$  Torr (top row);  $2.8 \times 10^{-2}$  Torr (middle row); atmospheric pressure (bottom row). The exposure time was  $t_w = 100$  ns. The timings in the images represent the time after the beginning of the laser pulse. All of the images are normalized to their maximum intensity being the pseudo-color scale indicated for each figure.

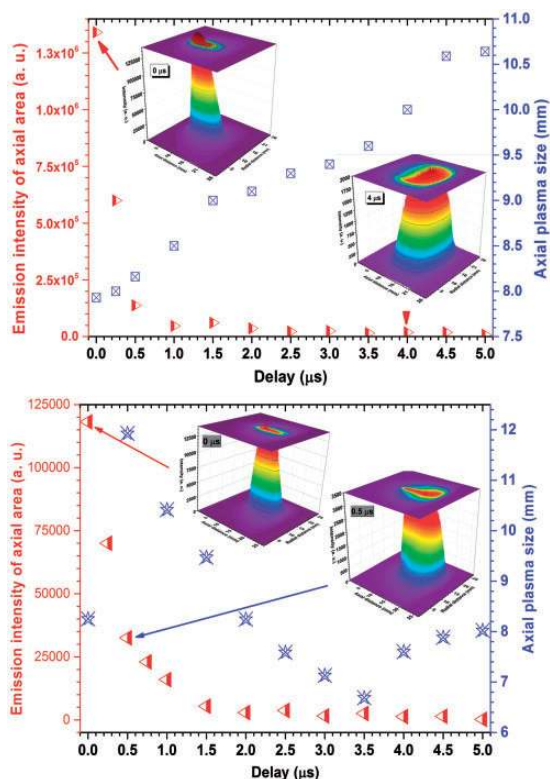


**Figure 2.** Emission intensity of axial area and axial plasma size (FWHM) at:  $7.5 \times 10^{-5}$  Torr (top figure);  $2.8 \times 10^{-2}$  Torr (bottom figure); as a function of time delay from the beginning of the laser pulse. Inset plots show images at different delays.

top row, and Figure 2, top panel), the interaction of the plasma with the ambient air becomes complicated because of new processes such as the formation of shock waves and clustering, plume splitting, reduction in ablation, confinement, deceleration of the plasma, thermalization, and diffusion.

By measuring the axial cross-sectional area and the axial size of the plasma (Figure 2, top panel), the decrease of the intensity and the growth of the plasma size was quantified over the range of delays. Emission intensities at  $7.5 \times 10^{-5}$  Torr as a function of axial and radial distances are given in Figure 3 (top panel). The inset in Figure 3 displays the normalized radial intensity profiles. For easier comparison, each profile has been normalized to its maximum intensity. The axial-distance zero corresponds to the target position. Low intensity radiation is observed at negative distances due to the penetration of the laser pulse on the sample and the reflection of the light from the sample surface. The axial emission intensity profiles ( $7.5 \times 10^{-5}$  Torr) show a single peak distribution for different delay times after plasma formation indicating uniform emission along the expansion direction. The LPP images show plume expansion up to  $\sim 20$  mm in both axial and lateral directions. The radial emission intensity profiles show a single peak

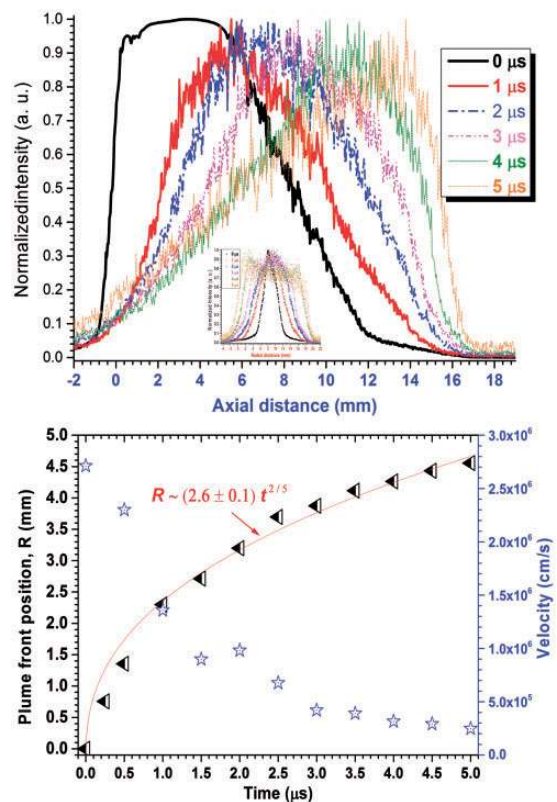


**Figure 3.** (Top panel) Normalized axial intensity profiles from the ICCD images of the plasma in vacuum ( $P_{\text{air}} = 7.5 \times 10^{-5}$  Torr) as a function of time delay. The inset shows the normalized radial intensity profiles; (bottom panel) distance–time ( $R-t$ ) plot and velocities obtained from the ICCD images of the plasma in vacuum ( $P_{\text{air}} = 7.5 \times 10^{-5}$  Torr) are given along with the fit to a shock wave model.

distribution for short delay times ( $t_d < 3.5 \mu\text{s}$ ) and splitting to two symmetrical maxima at long times.

The plasma expansion into vacuum background is adiabatic and can be predicted by theoretical models and numerical gas dynamics simulations.<sup>28</sup> The imaging data were used to generate position–time plots of the plasma front ( $7.5 \times 10^{-5}$  Torr) and the results are given in Figure 3 (bottom panel). The position of the plume-shock front boundary is found to be well defined in shadowgraphy images<sup>29</sup> while it is difficult to estimate in recording ICCD images due to the intense self-emission. As noted in Harilal et al.,<sup>29</sup> we took the plume front position based on a 90% reduction in the maximum intensity. The obtained data are plotted in Figure 3b along with a fit to the shock model. Since a distance threshold exists for the shock wave formation, we considered a delayed shock wave.<sup>30</sup> The plume front behaves linearly at early times ( $t_d < 0.5 \mu\text{s}$ ), indicating free expansion of the plume into vacuum. The expansion velocities of the plasma front were estimated from the slopes of the position–time plot. As we can see in the plots, there is no splitting of the plasma-plume and as

the time evolves, the maximum and the position of the shock front increase. In the vacuum and up to about 1  $\mu\text{s}$ , the plasma expansion is approximately linear and at later times there is a deceleration of the plume. The initial and maximum velocity of the expanding plasma is about  $3 \times 10^6$  cm/s and later decreases slowly up to  $0.25 \times 10^6$  cm/s at 5  $\mu\text{s}$ .

According to the Taylor–Sedov (TS) theory,<sup>30</sup> for a blast wave emanating from a strong point explosion, the shock position  $R$  is defined by:

$$R = \xi_0 \left( \frac{E_0}{\rho_b} \right)^{1/(n+2)} t^{2/(n+2)} \quad (1)$$

where  $\xi_0$  is a constant given by  $\xi_0 = [(75/16\pi)(\gamma-1)(\gamma+1)^2 / (3\gamma-1)]^{1/5}$   $\gamma$  being the adiabatic index,  $E_0$  the amount of energy released during the explosion,  $\rho_b$  the background gas density and  $t$  the delay time. The parameter  $n$  is 1 for a planar shock wave, 2 for cylindrical, and 3 for spherical. This model neglects viscosity and is applicable when the mass of the ejected material is small compared with the mass of the ambient gas set in motion by the shock wave. Therefore, a general equation of the form  $R(t) = a t^{0.4}$  is employed for modeling the spherical shock wave dynamics where  $a$  is a constant. Figure 3b shows an  $R$ – $t$  plot at  $7.5 \times 10^{-5}$  Torr along with the corresponding fit  $R \sim (2.6 \pm 0.1) t^{2/5}$  [mm/ $\mu\text{s}^{2/5}$ ]. The plot fit is better after 1  $\mu\text{s}$  in accordance with Figure 1 (top row). The validity of the shock wave model is restricted to a distance region where the mass of the gas surrounding the shock wave is higher than the ablated mass up to distances at which the pressure driving the moving of the plume is greater than the pressure of the gas at rest. The limiting spatial region  $R$  beyond the shock wave model is not valid is

$$\left( \frac{3M_p}{4\pi\rho_b} \right)^{1/3} \ll R \ll \left( \frac{E_0}{P_b} \right)^{1/3} \quad (2)$$

where  $M_p$  is the mass of the expanding plume and  $P_b$  is the pressure ahead of the shock wave front.<sup>31</sup> According to Zeldovich and Raiser,<sup>30</sup> the shock wave formation becomes important when the mass of the displaced gas is comparable to the mass of the plasma  $M_p$ . Assuming a hemispherical expansion of the plasma,  $M_p$  can be estimated by

$$M_p = \frac{2}{3} \pi R_{\text{SW}}^3 \rho_b \quad (3)$$

being  $R_{\text{SW}}$  the front radius.

### Drag Model in Expanding Plasma

Normalized intensities of axial area at  $2.8 \times 10^{-2}$  Torr obtained from the images given in Figure 1b as a function of axial distance are given in Figure 4 (top panel). The axial

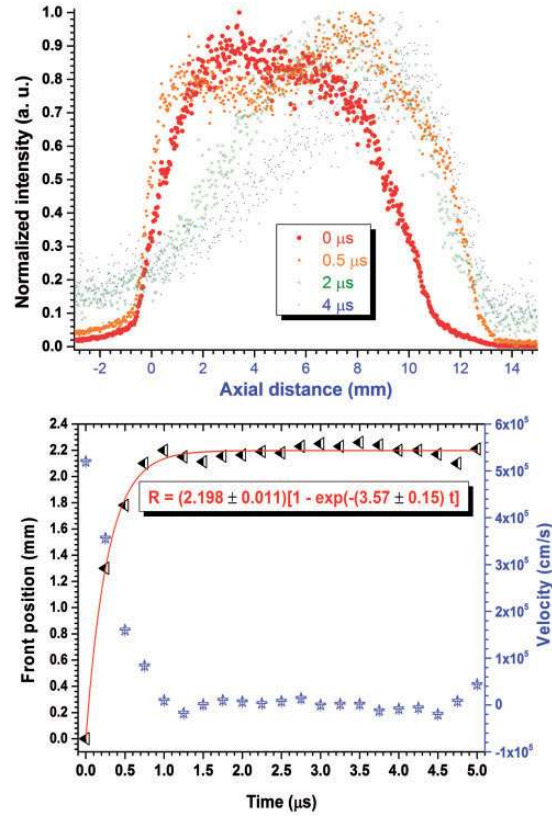


**Figure 4.** (Top figure) Normalized axial intensity profiles from the ICCD images of the plasma in medium vacuum ( $P_{\text{air}} = 2.8 \times 10^{-2}$  Torr) as a function of time delay; (bottom figure) distance–time ( $R$ – $t$ ) plot and velocities obtained from the ICCD images of the plasma in vacuum ( $P_{\text{air}} = 2.8 \times 10^{-2}$  Torr) are given along with the fit to a drag model.

emission intensity profiles display a single peak distribution for different delay times after plasma formation indicating uniform emission along the expansion direction. The LPP images (Figure 1, middle row) show plume expansion up to  $\sim 15$  mm in both axial and lateral directions. The imaging data were used to generate position–time plots of the plasma front at  $2.8 \times 10^{-2}$  Torr. At this pressure, the drag model<sup>31</sup> provides a better fit in a high viscous background ambient, which is given by

$$R = R_0(1 - e^{-\beta t}) \quad (4)$$

where  $R_0$  is the stopping distance of the shock wave of the plasma (distance at which the plume comes to rest) and  $\beta$  is the stopping coefficient. This model predicts that the plume will come to rest due to the resistance from collisions with the background gas. As time evolves, the plume slows down and the ejected particles collide with the ambient gas atoms and lose their kinetic energy. The expanding plume acts as a piston that compresses the ambient gas. The measured front position versus delay at  $2.8 \times 10^{-2}$  Torr is plotted in Figure 4 (bottom panel) along with a fit to the drag model.

Figure 4 shows that the drag model agrees well with our data points and the values of the fitting parameters are  $\beta = 3.57 \pm 0.15 \mu\text{s}^{-1}$  and  $R_0 = 2.198 \pm 0.011 \text{ mm}$ . The expansion velocities of the plasma front were estimated from the slopes of the position–time plot. Figure 8 shows that the initial plume velocity is  $5.2 \times 10^5 \text{ cm/s}$  and later decreases rapidly up to  $0.1 \times 10^5 \text{ cm/s}$  at  $1 \mu\text{s}$ , being approximately zero at higher times. By comparing the plume velocity at a higher vacuum (Figure 3), slow down is obvious due to the interaction of the plume with air molecules that creates a drag force. Moreover, there is a decrease in the ablated mass (as shown in the next section) and therefore in the generated laser-induced plasma.

Emission intensities of axial area and some 3D plasma images at atmospheric pressure as a function of the delay time are given in Figure 5 (top panel). The averaged images revealed that the plasma emission intensity decayed exponentially with time, but certain instabilities and plume splitting appear. Figure 5 (bottom panel) displays the normalized axial intensity profiles from the ICCD images of the plasma at atmospheric pressure as a function of time delay. The axial emission intensity profiles at atmospheric pressure

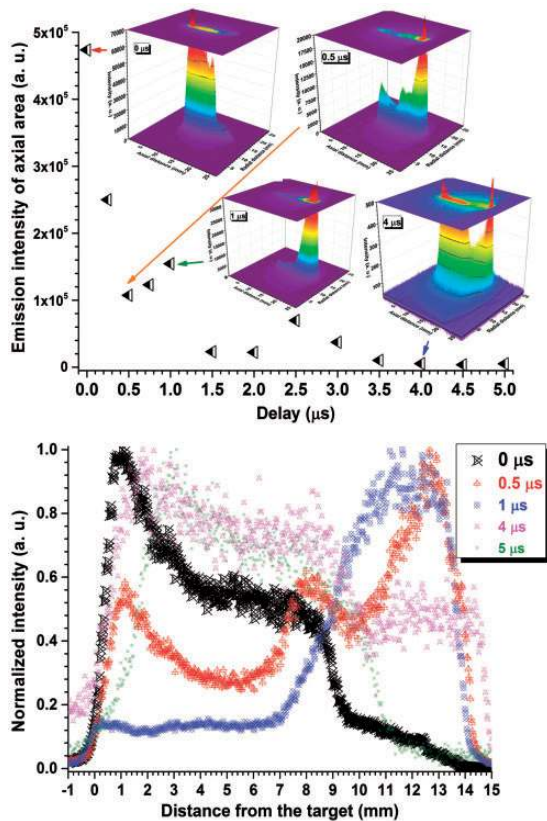


**Figure 5.** (Top figure) Emission intensity of axial plasma area at atmospheric pressure. Inset plots show four images at different delay times; (bottom figure) normalized axial intensity profiles from the ICCD images of the plasma at atmospheric pressure as a function of time delay.

show a multiple peak distribution for different delay times after plasma formation, indicating complex interactions among the plasma generated on the target, the plasma generated in the background air, etc. As we said before, at pressures close to one atmosphere, the plume breaks away from the target surface after the onset of the laser pulse, producing a slow moving or a quasi-steady component near the target and a faster moving component slighter out of the laser incident axis. The plasma behavior is described by a strong interpenetration and interaction of the plasma and the ambient high-pressure gas. A contact boundary region is formed between the plume and the shock wave in the gas. As before, the averaged-image intensities at atmospheric pressure (Figure 5) decay approximately exponentially with time. However, if we compare the plasma produced at  $2.8 \times 10^{-2} \text{ Torr}$  (Figures 1 and 2, middle panels), there is an increase in the intensity of this plasma at atmospheric pressure, although the measured ablated mass is lower. The increase in emission intensity of the expanding plasma in background gas can be attributed mainly from excitations due to collisions with background atoms and electron impact excitation/recombination. Between these two cases, electron impact processes should play the dominant role in excitation, as the cross-sections of atom–atom collision is two orders of magnitude lower than the electron–atom collisions.<sup>32</sup> The interaction between the expanding plume and the ambient gas can cause the ionization of ambient gas, which contributes to the increase in electron density. In addition, we have reported a decrease of the breakdown threshold intensity in air from 1 to  $0.3 \text{ GW} \times \text{cm}^{-2}$  for air pressures between 30 hPa and 500 hPa followed by an increase up to  $1.2 \text{ GW} \times \text{cm}^{-2}$  at atmospheric pressure.<sup>26</sup> For air pressures less than  $\sim 10 \text{ hPa}$ , air breakdown was not observed for a TEA-CO<sub>2</sub> laser with a maximum power density of  $\sim 6.3 \text{ GW} \times \text{cm}^{-2}$ . An increase in electron density, and hence

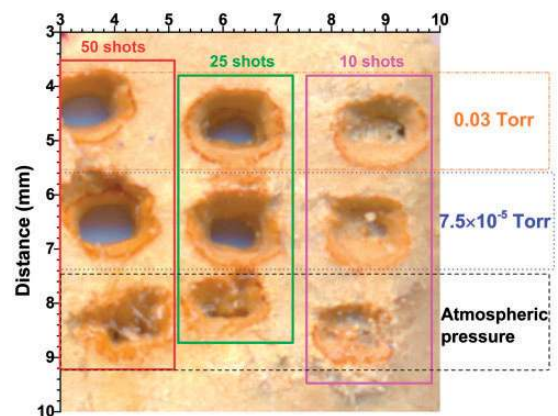


**Figure 6.** Photograph showing the swine muscle tissue surface characteristics after irradiating by 10, 25, and 50 laser pulses in vacuum ( $7.5 \times 10^{-5}$  and  $0.03 \text{ Torr}$ ) and atmospheric pressure.

increased electron impact excitation, could be responsible for the enhancement of emission at high pressures. Another factor, which accounts for the large difference in the emission intensity at  $2.8 \times 10^{-2}$  Torr and at atmospheric pressure, is the cascade growth of the electron number density and absorption coefficient of the plasma

in the ambient environment. The condition for the cascade growth is expressed as<sup>33</sup>

$$\left(\frac{d\varepsilon}{dt}\right) = \frac{4\pi^2 e^2 I v_{\text{eff}}}{m c \omega^2} - \frac{2m v_{\text{eff}}}{M_b} \quad (5)$$

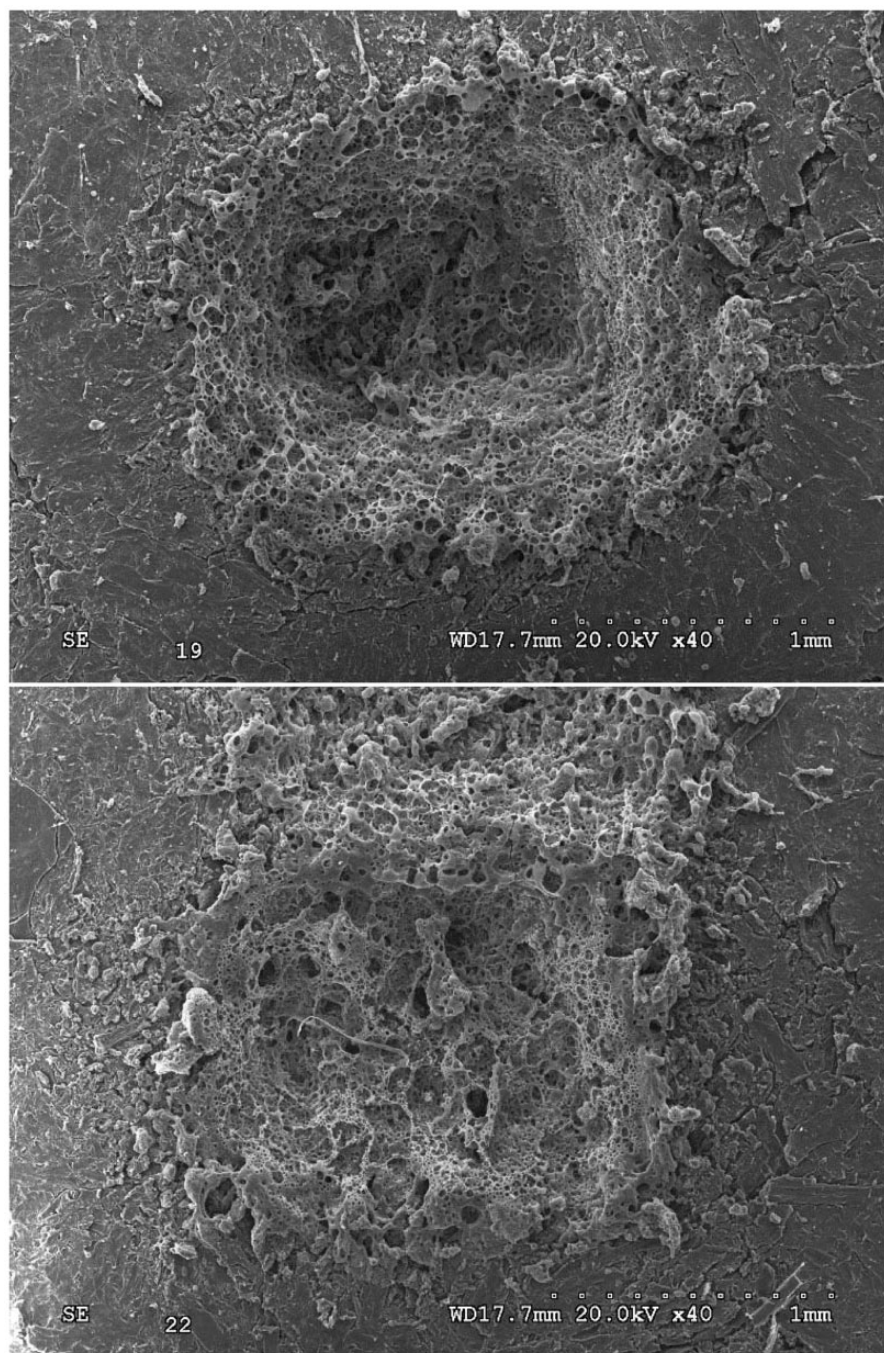


**Figure 7.** Scanning electron micrographs revealing the swine muscle tissue surface characteristics after irradiating by 10 laser pulses in two different vacuum conditions (75 [top] and 660 [bottom] Torr).

where  $\varepsilon$  is the energy of the free electrons,  $e$  and  $m$  are the charge and mass of the electron,  $M_b$  is the mass of the background gas neutral particle,  $I_P$  is the energy of the first ionization stage of the gas,  $\nu_{\text{eff}}$  is the effective frequency of electron-neutral collision,  $I$  is the laser radiation intensity, and  $\omega$  is the frequency of the laser radiation. The first term on the right-hand side of Eq. (5) expresses the rate of growth of energy by the absorption of laser photons and the second term gives the maximum rate of energy loss due to elastic and inelastic collisions with neutral gas particles. On comparing air at low and high pressure, the condition for cascade growth is more favorable at higher pressures than at lower pressures [ $M_b(4.67 \times 10^{-8} \text{ g/cm}^3$  at  $2.8 \times 10^{-2}$  Torr)  $\ll M_b(0.0011 \text{ g/cm}^3$  at 760 Torr) considering nitrogen]. This indicates that electron temperature and density of the plasma-plume should be higher at high pressures compared to low pressures. This will result in an increase in electron impact excitation, which is largely dependent on electron temperature and density. It should be noted that the cascade growth condition should not be favored at higher pressures ( $P > 1$  atm) because of the increased energy loss due to elastic collision of the electrons with the neutral particles of the gas.

### Ambient Air Effects on Crater Profiles

The interaction of a pulsed laser with a condensed phase material produces an ablation of mass which is partially evaporated and transferred into plasma, where the excited species emit element-specific radiation used for LIBS. A fraction of the ablated mass leaves the target as particle, liquid, or vapor. Later this vapor condenses in the neighborhood of the laser spot. The ejected particles may be carried away by the gas flow or propagate back to the laser-sample interaction region producing a deposition forming droplets or splashes. Due to the complexity of the involved processes, it is difficult to estimate quantitatively the ablated mass. However, the amount of removed mass can be estimated on the basis of the measured density of the sample and the volume of the crater, assuming that the plasma parameters are homogeneous inside the plasma and the ablated material is completely vaporized in plasma. Due to the low hardness of the tissue sample, crater formation was observed even after a single-shot laser pulse; nevertheless, we irradiated the samples with several shots in each spot to facilitate the measurement of physical parameters. Figure 6 shows a photograph of the crater profiles obtained after 10, 25, and 50 accumulated laser shots in two vacuum conditions ( $7.5 \times 10^{-5}$  and 0.03 Torr) and at atmospheric pressure. It is visible that the ambient gas pressure influences the amount of the laser-produced ablated material modifying both laser-target and laser-plasma coupling. In the vacuum, the sample, 1.5 mm thick, was perforated when irradiated with 25 or 50 shots. For a specific ambient pressure, as the pulse number increases, the crater depth and the ablated mass grow

approximately linearly. The measured diameters and depth of the different craters show that these parameters decrease as the ambient air pressure increases. Figure 7 shows the SEM images of the craters produced with 10 laser shots at two air pressures (75 and 660 Torr). The laser spots show a central intense melting region, where some amount of mass has been removed and an external region around it where are observed microstructures. There is a re-solidification of molten material in the form of a vortex, droplets, pores, and re-deposition of particles. As the laser intensity is highest at the center and decreases towards the periphery, it generates a temperature gradient which causes liquid material movement mainly along the radial direction, resulting in the formation of regular elevation (ripples) which spread up to the periphery of the laser spot. To calculate the ablated mass, we imagine the crater as an elliptic conical frustum, then measuring the upper diameters and depth we can calculate the bottom diameters and volume. For example, for the craters shown in Figure 7, the ablated mass at 75 Torr is three times greater than at 660 Torr (Table 1). The estimated uncertainty of the ablated mass determination is about 30%. In addition, a substantial splashing of molten material is prominent on the crater produced at a higher pressure (Figure 7). At higher pressures, the plasma shielding becomes dominant, which not only reduces the mass ablation, but also absorbs the energy from the incoming laser resulting into high temperature plasma in front of the target surface. This hot plasma may enhance the pressure on the molten surface, which may cause the splashing and enhances the material movement from center to periphery of treated area. Similar observations have been reported by Farid et al.<sup>34</sup>

### Scanning Electron Microscopy (SEM) and Energy-Dispersive X-ray Spectroscopy (EDX) Elemental Analysis of the Sample

The SEM-EDX chemical microanalysis is shown in Table 2. An almost similar composition was observed on the original surface of the sample and in the formed crater after

**Table 1.** Volume and ablated mass per pulse from craters of Figure 7.

Axis, depth (mm)	Pressure 75 Torr	Pressure 660 Torr
$d1$ (major axis upper ellipse)	2.04	1.64
$d2$ (minor axis upper ellipse)	1.64	1.10
$d3$ (major axis bottom ellipse)	1.78	1.48
$d4$ (minor axis bottom ellipse)	1.42	0.96
$h$ (crater depth)	0.42	0.26
Volume ( $\text{mm}^3$ )	0.966	0.328
Ablated mass ( $\mu\text{g/pulse}$ )	90	30

$$V = (h\pi/12) \times [(d1 \times d2) + (d3 \times d4) + (d1 \times d2 \times d3 \times d4)^{1/2}]$$

interaction with the laser. Nevertheless, other surface regions show important changes in elemental composition (study in progress). Other elements such as H (impossible to detect by EDS), Mg, and Ca were observed by LIBS.<sup>22,23</sup> The concentrations of all elements agree with the composition of

**Table 2.** Mean compositional analysis data from the swine muscle tissue sample.

Ele.	Series	Norm. Conc. <sup>a</sup> (wt. %)	At. Conc. <sup>a</sup> (wt. %)	Norm. Conc. <sup>b</sup> (wt. %)	At. Conc. <sup>b</sup> (wt. %)
C	K <sub>α</sub>	54.48 ± 1.92	61.19	52.88 ± 1.77	59.3
N	K <sub>α</sub>	16.55 ± 2.52	15.94	19.79 ± 2.30	19.0
O	K <sub>α</sub>	25.38 ± 1.23	21.40	24.23 ± 1.15	20.4
Na	K <sub>α</sub>	0.35 ± 0.08	0.21	0.36 ± 0.07	0.21
Si	K <sub>α</sub>	0.05 ± 0.04	0.02	–	–
P	K <sub>α</sub>	0.61 ± 0.10	0.26	0.62 ± 0.08	0.27
S	K <sub>α</sub>	0.83 ± 0.10	0.35	0.72 ± 0.08	0.30
Cl	K <sub>α</sub>	0.52 ± 0.06	0.20	0.19 ± 0.05	0.07
K	K <sub>α</sub>	1.23 ± 0.08	0.43	1.22 ± 0.08	0.42

<sup>a</sup>Without laser ablation

<sup>b</sup>After laser ablation (see Figure 8)

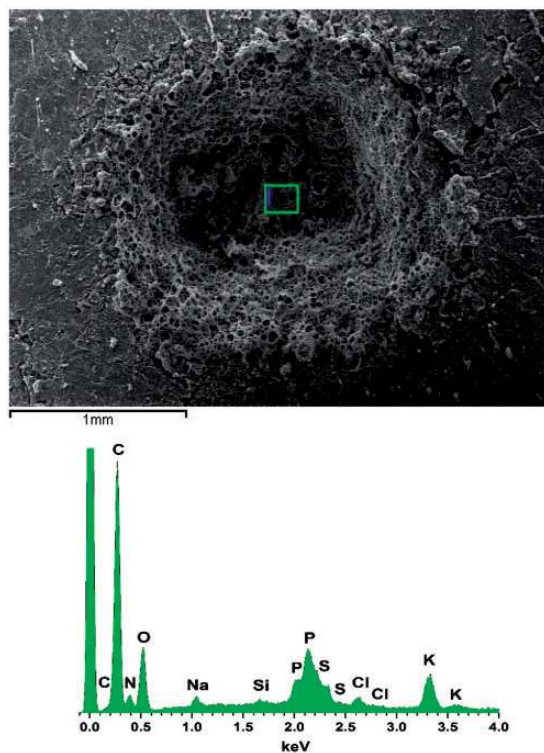


**Figure 8.** Scanning electron micrograph showing sample ablated surface characteristics (75 Torr) and its corresponding EDX microanalysis spectrum for the indicated area.

a dehydrated animal tissue. The minimum detection limit of an EDX analyzer is approximately 0.1% for elements with  $Z > 10$  and about 1.0 wt. % (weight percentage) for lighter elements.<sup>35</sup> In EDX, the majority of X-ray emission is originated from a volume beneath the sample surface. In the analysis reported here (Table 2 and Figure 8), the calculated electron penetration of the X-rays is about 7.3  $\mu\text{m}$ .

## Conclusions

The plasma-plume expansion dynamics of an ablated swine muscle tissue target by CO<sub>2</sub> pulsed laser at 10.591  $\mu\text{m}$  has been investigated in different ambient air pressures. Measurements were made using high-speed photography imaging. The laser intensity was fixed at 1.1  $\text{GW} \times \text{cm}^{-2}$  and the surrounding ambient air was varied from vacuum ( $7.5 \times 10^{-5}$  Torr) to atmospheric pressure. The imaging data were used to generate 2D position–time plots of the luminous plasma-front. Effects such as plume splitting, sharpening, and stopping were observed depending on the air pressure. The position and velocity of the plume front were determined and fitted to a shock wave or drag model depending on vacuum conditions. Plume profile was depending on the surrounding ambient pressure. The ablated mass was calculated, increasing for low pressure. The effect of the number of laser shots on the crater volume at different ambient air pressures was also studied. We examined swine muscle tissues combining SEM with EDX to visualize and analyze different regions of the sample.

## Conflict of Interest

The authors report there are no conflicts of interest.

## Funding

The authors gratefully acknowledge the support received in part by the DGICYT (Spain) Project MICINN: CTQ2013-43086 for this research.

## References

1. D. Chrisey, G.K. Hubler (eds) Pulsed Laser Deposition of Thin Films. New York, NY: Wiley, 1994.
2. D.E. Motaung, M.K. Moodley, E. Manikandan, N.J. Coville. *J. Appl. Phys.* 2010. 107(4): 044308–15 **AQ1**.
3. M.S. Brown, C.B. Arnold. "Fundamentals of Laser–Material Interaction and Application to Multiscale Surface Modification". In: K. Sugioka, M. Meunier, A. Pique (eds) *Laser Precision Microfabrication*. Springer Series in Materials Science, Chap. 4. Berlin: Springer, 2010, pp.91–120.
4. D.A. Cremers, L.J. Radziemski. *Handbook of Laser-Induced Breakdown Spectroscopy*. New York, NY: Wiley, 2006.
5. D.W. Hann, N. Omenetto. "Laser-Induced Breakdown Spectroscopy (LIBS), Part I: Review of Basic Diagnostics and Plasma-Particle Interactions: Still-Challenging Issues Within the Analytical Plasma Community". *Appl. Spectrosc.* 2010. 64(12): 335–366.
6. D.W. Hann, N. Omenetto. "Laser-Induced Breakdown Spectroscopy (LIBS), Part II: Review of Instrumental and Methodological Approaches to Material Analysis and Applications to Different Fields". *Appl. Spectrosc.* 2012. 66(4): 347–419.

7. R. Noll. *Laser-Induced Breakdown Spectroscopy: Fundamentals and Applications*. New York, NY: Springer, 2012.
8. S. Musazzi, U. Perini. *Laser-Induced Breakdown Spectroscopy. Theory and Applications*. Heidelberg: Springer, 2014.
9. K. Krushelnick, E.L. Clark, R. Allott, F.N. Beg, C.N. Danson, A. Machacek, V. Malka, Z. Najmudin, D. Neely, P.A. Norreys, M.R. Salvati, M.I.K. Santala, M. Tatarakis, I. Watts, M. Zepf, A.E. Dangor. *IEEE Transactions on Plasma Science*. 2000. 28(4): 1110–1155 **[AQ1]**.
10. S.S. Harilal, T. Szyuk, A. Hasanein, D. Campos, P. Hough, V. Szyuk. "The Effect of Excitation Wavelength on Dynamics of Laser-Produced Tin Plasma". *J. Appl. Phys.* 2011. 109: 063306–066309.
11. S.S. Harilal, G.V. Miloshevsky, T. Szyuk, A. Hasanein. "Effects of Excitation Wavelength on Ly- $\alpha$  and He- $\alpha$  Line Emission from Nitrogen Plasmas". *Phys. Plasmas*. 2013. 20(1): 013105.
12. J. Meijer. "Laser Beam Machining (LBM), State of the Art and New Opportunities". *Journal of Materials Processing Technology*. 2004. 149: 2–17.
13. C.A. Munson, F.C. De Lucia, T. Piehler, K.L. McNesby, A.W. Miziolek. "Investigation of Statistics Strategies for Improving the Discriminating Power of Laser-Induced Breakdown Spectroscopy for Chemical and Biological Warfare Agent Simulants". *Spectrochim. Acta Part B*. 2005. 60(7–8): 1217–1224.
14. J.L. Gottfried, F.C. De Lucia, C.A. Munson, A.W. Miziolek. "Standoff Detection of Chemical and Biological Threats Using Laser-Induced Breakdown Spectroscopy". *Appl. Spectrosc.* 2008. 62(4): 353–363.
15. D. Santos, R.E. Samad, L.C. Trevizan, A.Z. Freitas, N.D. Vieira, F.J. Krug. "Evaluation of Femtosecond Laser-Induced Breakdown Spectroscopy for Analysis of Animal Tissues". *Appl. Spectrosc.* 2008. 62(10): 1137–1143.
16. R. Kanawade, F. Mehari, C. Knipfer, M. Rohde, K. Tangermann-Gerk, M. Schmidt, F. Stelzle. "Pilot Study of Laser Induced Breakdown Spectroscopy for Tissue Differentiation by Monitoring the Plume Created During Laser Surgery - An Approach on a Feedback Laser Control Mechanism". *Spectrochim. Acta, Part B*. 2013. 87(1): 175–181.
17. J.D. Hybl, G.A. Lithgow, S.G. Buckley. "Laser-Induced Breakdown Spectroscopy Detection and Classification of Biological Aerosols". *Appl. Spectrosc.* 2003. 57: 1207–1215.
18. M. Baudelet, M. Boueri, J. Yu, S.S. Mao, V. Piscitelli, X. Mao, R.E. Russo. "Time-Resolved Ultraviolet Laser-Induced Breakdown Spectroscopy for Organic Material Analysis". *Spectrochim. Acta Part B*. 2007. 62(12): 1329–1334.
19. H. Jelinkova. *Laser for Medical Applications: Diagnostics, Therapy and Surgery*. Cambridge, UK: Woodhead Publishing, 2013.
20. S.S. Harilal, C.V. Bindhu, M.S. Tillack, F. Najmabadi, A.C. Gaeris. "Internal Structure and Expansion Dynamics of Laser Ablation Plumes into Ambient Gases". *J. Appl. Phys.* 2003. 93(5): 2380–2388.
21. S. Lafane, T. Kerdja, S. Abdelli-Messaci, S. Malek, M. Maaza. "Laser-Induced Plasma Study by Fast Imaging for Sm<sub>1-x</sub>Nd<sub>x</sub>NiO<sub>3</sub> Thin Film Deposition". *Appl. Appl. A*. 2010. 98(2): 375–383.
22. J.J. Camacho, L. Diaz, S. Martinez-Ramirez, J.O. Caceres. "Time- and Space-Resolved Spectroscopic Characterization of Laser-Induced Swine Muscle Tissue Plasma". *Spectrochim. Acta Part B*. 2015. 111: 92–101.
23. A. Marin-Roldan, S. Manzoor, S. Moncayo, F. Navarro-Villoslada, R.C. Izquierdo-Hornillos, J.O. Caceres. "Determination of the Postmortem Interval by Laser Induced Breakdown Spectroscopy Using Swine Skeletal Muscles". *Spectrochim. Acta Part B*. 2013. 88: 186–191.
24. J.J. Camacho, M. Santos, L. Diaz, L.J. Juan, J.M.L. Poyato. "Spectroscopy Study of Air Plasma Induced by IR CO<sub>2</sub> Laser Pulses". *Appl. Phys. A*. 2010. 99: 159–175.
25. J.J. Camacho, L. Diaz, J.M.L. Poyato. "Time-Resolved Spectroscopic Diagnostic of Laser-Induced Plasma on Germanium Targets". *J. Appl. Phys.* 2011. 109(10): 103304–103304-5.
26. J.J. Camacho, L. Diaz, M. Santos, J.M.L. Poyato. "Time-Resolved Optical Emission Spectroscopic Measurements of He Plasma Induced by a High-Power CO<sub>2</sub> Pulsed Laser". *Spectrochim. Acta Part B*. 2011. 66: 57–66.
27. L. Diaz, J.J. Camacho, J.P. Cid, M. Martin, J.M.L. Poyato. "Time Evolution of the Infrared Laser Ablation Plasma Plume of SiO". *Appl. Phys. A*. 2014. 117(1): 125–129.
28. R.K. Singh, J. Narayan. "Pulsed-Laser Evaporation Technique for Deposition of Thin Films: Physics and Theoretical Model". *Phys. Rev. B*. 1990. 41: 8843–8859.
29. S.S. Harilal, G.V. Miloshevsky, P.K. Diwakar, N.L. LaHaye, A. Hassanein. "Experimental and Computational Study of Complex Shockwave Dynamics in Laser Ablation Plumes in Argon Atmosphere". *Phys. Plasmas*. 2012. 19(8): 083504.
30. Y.B. Zeldovich, Y.P. Raizer. *Physics of Shock Waves and High-Temperature Hydrodynamics Phenomena*. New York, NY: Dover, 2002.
31. P.E. Dyer, J. Sidhu. "Spectroscopic and Fast Photographic Studies of Excimer Laser Polymer Ablation". *J. Appl. Phys.* 1988. 64: 4657–4663.
32. J.C.S. Kools. "Monte Carlo Simulations of the Transport of Laser-Ablated Atoms in a Diluted Gas". *J. Appl. Phys.* 1993. 74(10): 6401–6406.
33. G.M. Weyl. "Laser-Induced Plasmas and Applications". In: L.J. Radziemski, D.A. Cremers (eds) **[AQ2]**, Chap. 1. New York: Dekker, 1989.
34. N. Farid, S.S. Harilal, H. Ding, A. Hassanein. "Emission Features and Expansion Dynamics of Nanosecond Laser Ablation Plumes at Different Ambient Pressures". *J. Appl. Phys.* 2014. 115(3): 033107.
35. C.R. Brundle, C.A. Evans, S. Wilson. *Encyclopaedia of Materials Characterization: Surfaces, Interfaces and Thin Films*. Boston, MA: Butterworth Heinemann, 1992.